

Buckling and its effect on the confined flow of a model capsule suspension

Spencer H. Bryngelson¹ · Jonathan B. Freund^{1,2}

Received: 30 May 2015 / Revised: 12 November 2015 / Accepted: 13 December 2015 / Published online: 5 January 2016
© Springer-Verlag Berlin Heidelberg 2016

Abstract The rheology of confined flowing suspensions, such as blood, depends upon the dynamics of the components, which can be particularly rich when they are elastic capsules. Using boundary integral methods, we simulate a two-dimensional model channel through which flows a dense suspension of fluid-filled capsules. A parameter of principal interest is the equilibrium membrane perimeter, parameterized by ξ_o , which ranges from round capsules with $\xi_o = 1.0$ to $\xi_o = 3.0$ capsules with a dog-bone-like equilibrium shape. It is shown that the minimum effective viscosity occurs for $\xi_o \approx 1.6$, which forms a biconcave equilibrium shape, similar to a red blood cell. The rheological behavior changes significantly over this range; transitions are linked to specific changes in the capsule dynamics. Most noteworthy is an abrupt change in behavior for $\xi_o \approx 2.0$, which correlates with the onset of capsule buckling. The buckled capsules have a more varied orientation and make significant rotational (rotlet) contributions to the capsule–capsule interactions.

Keywords Numerical simulation · Suspensions · Blood · Capsules

This paper belongs to the special issue on the “Rheology of blood cells, capsules and vesicles”.

✉ Jonathan B. Freund
jbfreund@illinois.edu

Spencer H. Bryngelson
bryngel2@illinois.edu

¹ Mechanical Science and Engineering, University of Illinois at Urbana-Champaign, Urbana, IL 61801, USA

² Aerospace Engineering, University of Illinois at Urbana-Champaign, Urbana, IL 61801, USA

Introduction

Rheology of suspensions depends upon the mechanics of the suspended elements, which can be particularly complex for elastic capsules, especially when flowing in narrow confines. In such cases, the membrane deformations can be strongly coupled with the overall flow dynamics (Zhou and Pozrikidis 1995; Ghigliotti et al. 2010; Lei et al. 2013; Freund 2014) making it difficult to analyze. We consider a simple model suspension of such capsules, each an incompressible liquid filled elastic membrane. These can be considered models of natural capsules, such as vesicles, biological cells, or viruses, or artificial capsules such as those used for targeted drug delivery or time releasing aromas or flavors (Clausen et al. 2011; Gibbs et al. 1999; Dey et al. 2008; Pop 2011; Paret et al. 2015). Natural capsules are typically formed by a lipid bi-layer membrane, which is buttressed in many cases with additional molecular components such as proteins. Common artificial membranes are manufactured using polymers such as alginate, poly-L-lysine, or polyacrylates (Ulbricht 2006). While these molecular details are important for the dynamics of any particular capsule system, we focus our study specifically on the finite-deformation dynamics of highly deformable membranes and do not further consider their molecular make-up.

Blood is a particularly important suspension of this type, and though we only consider a two-dimensional model configuration, it does reproduce an important phenomenology, quantitatively in cases; potential implications for the flow of blood cells in tight confines are discussed throughout. The baseline configuration we consider displays a biconcave equilibrium shape similar to a red blood cell (Jenkins 1977; Shiga et al. 1990; Smith et al. 1980; Canham 1970). We also consider capsules with increased

and decreased relative surface area, which corresponds to certain pathological conditions in blood. Both surface area and volume are approximately constant for healthy red blood cells, but some disease conditions cause relative volume to disproportionately increase forming spherocytes (e.g., Da Costa et al. 2013) or decrease forming sickle-shaped cells (e.g., Anderson et al. 1963; Li et al. 2013). Similarly, shape and mechanical properties are potentially important design parameters for artificial capsules to be suspended in blood or used otherwise (Peyratout and Dahne 2004; Raghunathan et al. 1981; Wang et al. 2008; Fedosov et al. 2014), and the development of artificial blood remains a long-term goal (Chang 2010). In our study, we consider a range of equilibrium shapes, loosely based upon those observed physiologically and potential variations, which lead to phenomenological changes in the capsule dynamics and thus the confined-suspension rheology.

The rheological behavior of such a suspension flowing in a narrow channel is most obviously manifested in its effective viscosity, as would be deduced based on pressure drop were it a homogeneous Newtonian fluid. For blood, complex scale-dependent behavior of effective viscosity has been observed for a long time (Martini et al. 1930; Fahraeus and Lindqvist 1931), the root mechanism of which seems to be the formation of a cell-free layer at adjacent walls. The formation of a cell-free layer decreases flow resistance and is thought to be an important factor in microcirculatory dynamics (Pries et al. 1992). The thickness of this cell-free layer has been shown to decrease with increasing hematocrit, increase with increasing flow rate, and decrease with increasing cell membrane stiffness (Bugliarello and Sevilla 1970; Cokelet 1972; Sharan and Popel 2001; Srivastava 2007; Sankar and Lee 2008). We show a fundamental change in this layer for increasing membrane surface area: the overall viscous resistance increases abruptly with a concomitant disappearance of any significant capsule-free layer. The implications of this potentially extend beyond the overall rheology since the properties of red blood cells are also known to mediate the margination process of leukocytes and platelets (Skalak et al. 1989; Firrell and Lipowsky 1989; Zhao and Shaqfeh 2011; Kumar et al. 2014; Henriquez Rivera et al. 2015), which are important for inflammation and thrombosis.

Our goal is to quantify the effective viscosity, which potentially depends upon the capsule's reduced volume, and understand how this rheological behavior relates to the dynamics of the suspended elastic capsules. In particular, we investigate changes that occur as capsule equilibrium shapes are varied from relatively circular to very elongated, and how the microstructural dynamics of these capsules are manifested in the macroscopic suspension dynamics. This is done with a detailed, though two-dimensional, flow configuration, which serves as model for blood and its flow,

either in the microcirculation or in a microfluidic device. While this two-dimensional model will not necessarily be quantitatively precise for blood, or indeed any genuinely three-dimensional suspension, such a model has been used extensively to study capsule dynamics in homogeneous shear (Zhou and Pozrikidis 1995; Rahimian et al. 2010) and to reproduce key phenomena of the microcirculation (Freund 2007; Isfahani 2008). Its advantage is that it facilitates simulation of many cases and more extensive averaging to collect important flow statistics, which is helpful for discovering and mapping flow mechanisms and regimes.

The specific flow configuration studied is introduced in the “[Model capsule flow system](#)” section, and the spectral boundary integral method used to solve the fully-coupled fluid-structure capsule dynamics is outlined in the “[Numerical methods](#)” section. The results are discussed in the “[Results](#)” section, which includes the rheological changes in the suspension effective viscosity and the microstructural changes of the suspended capsules. This section also includes auxiliary simulations to quantify a capsule buckling behavior that is linked to the overall suspension dynamics and is reflected in a rapid increase in the role of capsule rotation in the overall dynamics, as quantified by a multipole expansion analysis. The section summarizes the principal conclusions and provides additional discussion regarding their implications.

Model capsule flow system

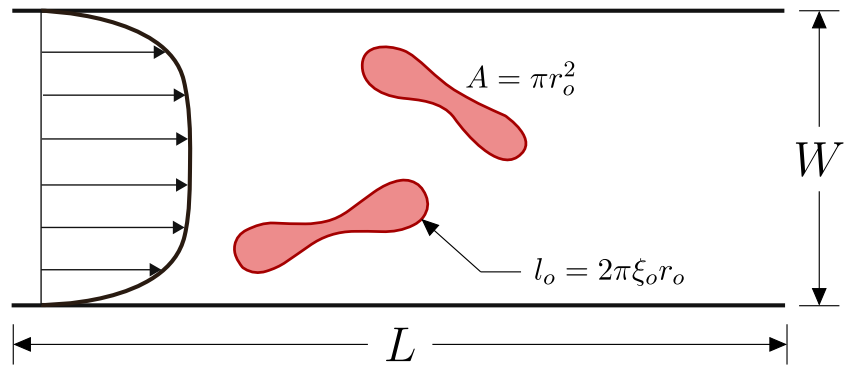
We consider a streamwise periodic channel as a model for fully developed flow in a long section of a microvessel or microfluidic device as shown in Fig. 1. The mean flow velocity is U , the channel width is W , its periodic length is L , and in it are N suspended capsules, each of area $A = \pi r_0^2$. For all quantitative results, $L = 40r_0$, which is sufficiently large that the reported results are insensitive to it. This was confirmed by doubling L and N for selected cases and confirming that effective viscosity statistics were unchanged. Channel widths vary from $W = 14r_0$ to $40r_0$. The area-fraction of the channel occupied by the capsules, a nominal hematocrit was this blood, is

$$H_c = \frac{N\pi r_0^2}{WL}, \quad (1)$$

which is varied $H_c = 0.01$ to 0.4 , covering a wide range from dilute to approximately that of whole blood.

The capsules are encased by elastic membranes with linear finite-deformation tension and bending moduli, T and M , respectively. This linearization is derived from the full nonlinear Helfrich energy (Cantat and Misbah 1999) and

Fig. 1 Schematic of the two-dimensional streamwise-periodic model channel with capsules of area A and perimeter l_o



has been employed previously for thin elastic membranes (Freund 2007; Pozrikidis 2001). We also verify by direct comparisons that the key reported observables changed by at most 4 % upon using the full nonlinear Helfrich energy. In terms of an arc length coordinate $s(s_o)$ and reference arc length s_o , the membrane tension τ and bending moment b are,

$$\tau = T \left(\frac{ds}{ds_o} - 1 \right) \quad \text{and} \quad b = M(C - C_o), \quad (2)$$

where C is the curvature with reference curvature $C_o = 0$. With these, the net traction exerted by the cells on the fluid is

$$\Delta\sigma = \frac{\partial t\tau}{\partial s} + \frac{\partial}{\partial s} \left(\frac{\partial b}{\partial s} \mathbf{n} \right), \quad (3)$$

where \mathbf{t} is the membrane unit tangent and \mathbf{n} is its outward unit normal. Of particular interest is the membrane reference length l_o relative to its minimum (that of a circle), which is parameterized by ξ_o : $l_o = 2\pi\xi_o r_o$. As such, ξ_o is the squared inverse of what might be considered a reduced area,

$$A_r = \frac{4\pi [\text{area}]}{[\text{perimeter}]^2} = \frac{1}{\xi_o^2}, \quad (4)$$

though we will generally quote ξ_o because of its clear connection with the capsule reference perimeter and therefore the buckling criterion (see “[Buckling](#)”).

The fluid both inside and outside the capsules is Newtonian with viscosity μ . Actual red blood cells are thought to have an elevated interior viscosity (Bronzino 2000; Whitmore 1968), by about a factor of 5 (Distenfass 1968), though matched viscosity has been shown to produce qualitatively realistic blood flow phenomena in two dimensions (Freund 2007) and quantitative accuracy for many quantities in three dimensions (Freund and Orescanin 2011). Taking values appropriate for blood under physiological conditions, the Reynolds number based upon the mean flow $U \lesssim 1$ mm/s, mass density $\rho = 10^3$ kg/m³, $\mu \approx 3 \times 10^{-3}$ Pa s, and $W = 30$ μ m is $Re \approx 0.01$, which supports neglect of inertia in the governing equations. We assume that any corresponding manufactured capsule

suspensions or microfluidic devices operate under similarly low-Reynolds-number conditions. For convenience, we form the parameters into a capillary number

$$u^* \equiv \frac{\mu U}{T}, \quad (5)$$

which we vary from $u^* = 0.2$ to 1 and can be interpreted as a ratio of an advection time to a relaxation time. Similarly, we define a relative stiffness parameter,

$$\frac{r_o^2 T}{M} = 50, \quad (6)$$

which we hold fixed at this relatively large value as a model for the near incompressibility of typical capsule membranes.

Numerical methods

The discretization is based upon a boundary integral representation for the velocity u_i in terms of the surface tractions from Eq. 3 (Pozrikidis 1992; Kim and Karrila 1991):

$$u_i(\mathbf{x}) = U_i(\mathbf{x}) + \frac{1}{4\pi\mu} \int_{\Omega} S_{ij}(\mathbf{y} - \mathbf{x}) \Delta\sigma_j(\mathbf{y}) ds(\mathbf{y}), \quad (7)$$

where $\mathbf{U}(\mathbf{x}) = (U, 0, 0)$ is the mean velocity and Ω represents the membranes and vessel walls with outward unit normal \mathbf{n} . The kernel S_{ij} of the integral in Eq. 7 is the Green’s function of the Stokes equation (the so-named Stokeslet),

$$S_{ij}(\mathbf{x}) = \frac{\hat{x}_i \hat{x}_j}{r^2} - \delta_{ij} \ln r, \quad (8)$$

evaluated at \mathbf{x} for a singular unit-strength Stokeslet force at \mathbf{x}' , with $\hat{\mathbf{x}} \equiv \mathbf{x} - \mathbf{x}'$ and $r \equiv |\hat{\mathbf{x}}|$.

Each membrane is discretized by N_p points distributed uniformly over its (periodic) reference arc length, parameterized by s_o . Derivatives and integrals on the membranes are computed via an interpolating Fourier series (Freund and Zhao 2010; Zhao et al. 2010). Though the Stokes flow (7) and constitutive model (2) are linear, the geometric factors (normals, tangents, and curvatures) introduce non-linearity, which can lead to numerical instability via aliasing

(Zhao et al. 2010; Freund 2014). This is suppressed, without compromising the fidelity of the solution supported by the Nyquist limit of the N_p collocation points, by evaluating $\Delta\sigma(s_o)$ on $N_a > N_p$ points and Fourier filtering to N_p points after nonlinear operations. In all simulations $N_a = 4N_p$. We confirm that reported results are insensitive to the selected resolution N_p .

To avoid both the complexity of a series of Green's functions to represent the walls (Weinbaum and Ganatos 1990; Staben et al. 2003) and the solution of a single-layer formulation, we enforce the no slip condition using a penalty method in which the wall is constructed from elements that are permitted to displace a small amount. Each of the 750 independent Δs_w -wide elements of each wall is anchored to its reference location \mathbf{x}_w by a Hookean spring, so its imposed traction is

$$\Delta\sigma_w = -S_w(\mathbf{x} - \mathbf{x}_w). \quad (9)$$

The spring constant $S_w = 1.7T/r_o^2$ can be relatively large without restricting the stability limit of the time integrator as set by the capsule membrane dynamics.

Consistent with the neglect of inertia in the flow equations the capsule membranes and vessel walls are assumed to be massless, so given the velocity $\mathbf{u}(\mathbf{x})$ from Eq. 7, the membrane position is governed simply by

$$\frac{d\mathbf{x}}{dt} = \mathbf{u}(\mathbf{x}), \quad (10)$$

which is applied to each collocation point of the discrete representation. This system (10) is integrated in time using a second-order Runge–Kutta scheme with a time step of $\Delta t = 0.01\mu r_o/T$.

It is well understood that the lubrication layers that form upon close approach between such capsules would mathematically prohibit contact in finite time for finite forces. However, even in our idealized physical model, numerical errors can lead to overlap between the capsules, which we avoid with a short-range repulsion between nearby capsules. Though this can be considered as a model for repulsive lubrication forces, physiologic capsules are expected to have more complex interactions, so it is unclear that even a precise lubrication formulation would be appropriate. Steric and electrostatic repulsions are thought to mediate contact between red blood cells at very small length scales (Jan and Chien 1973). For realistic simulation of blood cells in three dimensions, boundary integrals have been used to simulate lubrication down to the scale of proteins (Freund and Orescanin 2011), but further resolution is unlikely to provide a more realistic physical description because it would not represent in detail the actual contact and near-contact

interactions. In our formulation, the repulsion force at a point \mathbf{x} on a membrane due to another (\mathbf{x}') is

$$\mathbf{f}(\mathbf{x}) = \begin{cases} S_f \frac{e^{\delta-r}-1}{e^\delta-1} \frac{\mathbf{x}-\mathbf{x}'}{r} & \text{for } r \leq \delta \\ 0 & \text{otherwise} \end{cases}, \quad (11)$$

where $r = |\mathbf{x} - \mathbf{x}'|$, $\delta = 0.2r_o$, and $S_f = 2.5T$. The derivative of \mathbf{f} with respect to s is added to the traction (3) in the integrand of Eq. 7. Similarly, the area of the capsules is only enforced by the fidelity of the numerical schemes. Although this is very accurate because it is a low-order moment of the capsule shape and thus well resolved, still a weak variational correction is applied to preserve constant area indefinitely as has been used previously (Freund 2007).

Our implementation has been extensively verified against analytical results for Poiseuille flow in a wavy-walled channel (Isfahani 2008) and more recently for the drag on an infinite periodic lattice of circles in cross-flow (Hasimoto 1959). In this latter case, results are within 1 % error for 50 collocation points and 0.4 % error for 100 collocation points per circle. We also confirmed that the effective viscosity we report changed by less than 1 % upon changing the wall strength from $S_w = 1.7T/r_o^2$ to $3.4T/r_o^2$, repulsion from $S_f = 2.5T$ to $5T$, and both doubling and halving the repulsion length scale δ .

Results

Equilibrium shapes

We start by visualizing the equilibrium shapes for different ξ_o in Fig. 2, which display expected variations (Knoche and Kierfeld 2011; Brezavscek et al. 2012; Jenkins 1977).

ξ_o	Shape	Visualization
1.0	Circle	
1.3	Prolate	
1.4	Prolate-biconcave transition	
1.6	Biconcave	
1.8	Biconcave	
2.1	Biconcave-dog-bone transition	
2.4	Small aspect-ratio dog-bone	
3.0	Large aspect-ratio dog-bone	

Fig. 2 Example equilibrium shapes for different ξ_o

Taking $\xi_0 = 1.0$ yields a circle, which is only ever slightly distorted by flow for our conditions, and small increases in ξ_0 lead to a mildly prolate convex geometry. Increasing elongated prolate shapes for larger ξ_0 transition to a biconcave configuration near $\xi_0 \approx 1.4$, nominally matching a healthy red blood cell when $\xi_0 \approx 1.6$. Increasing ξ_0 further leads to additional inflection points for $\xi_0 \gtrsim 2.1$ and produces dog-bone-like shapes with increasingly large aspect ratios. Note that the repulsion force f between sufficiently close collocation points, according to (11), prevents the membrane from self-intersecting for large ξ_0 , as it would otherwise.

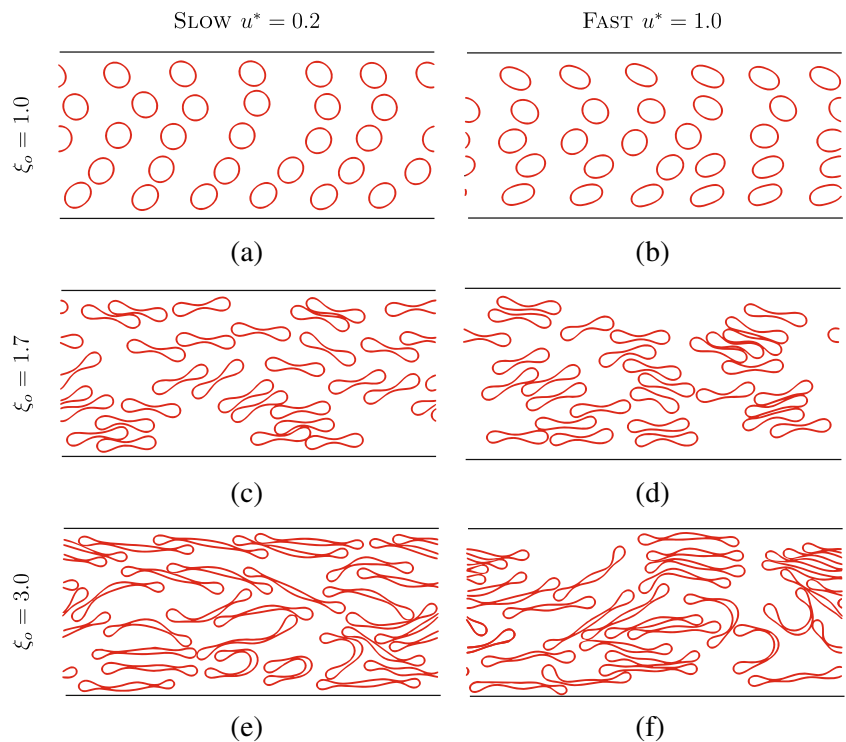
While $\xi_0 \approx 1.6$ corresponds most closely to a healthy red blood cell, the near-circular capsule geometry ($\xi_0 \approx 1.0$) is characteristic of spherocytes, the defining symptom of spherocytosis, a hereditary disorder that mutates the genes encoding red cell membrane proteins, causing a loss of membrane (Shiga et al. 1990; Chabanel et al. 1987). Additionally, many artificial capsules are manufactured to have a similar spherical shape (Dey et al. 2008; Majeti and Kumar 2000; Peyratout and Dahne 2004; Raghunathan et al. 1981; Wang et al. 2008). With increasing ξ_0 , the capsules become elliptical and prolate. These geometries are similar to those of elliptocytes, which are found in those diagnosed with elliptocytosis, caused by similar mutations as spherocytosis, but arise via lateral interactions of the cytoskeleton (Shiga et al. 1990; Chabanel et al. 1987). For larger $\xi_0 \gtrsim 2.0$, corresponding configurations for red blood cells have been observed in severe cases of anemia and sickle cell

anemia (Emmel 1917; d’Onofrio and Zini 2014). Manufactured capsules of this geometry have also been proposed for a variety of applications, such as coatings, aerosols, and drug delivery (Calle et al. 2012; Donbrow 1991) with different conformations. The behavior of these different capsules in flow is considered next.

Flow visualizations

Figure 3 shows flowing capsules for different ξ_0 at the smallest and largest capillary numbers. In the $\xi_0 = 1.0$ circular limit (Fig. 3a, b), capsules are only slightly deformed from circular shapes, though more so for the faster flow and nearer to the vessel walls where the shear stress is larger. The asymmetry of near-wall capsules is thought to facilitate their locomotion towards the center of a channel, which is known as shear-induced migration (Bishop et al. 2001; Freund and Orescanin 2011). For the $\xi_0 = 1.7$ cases with biconcave equilibrium shapes, capsules in Fig. 3c and d do not show any significant shape distortion for the range of capillary numbers simulated. In the large $\xi_0 = 3.0$ cases (Fig. 3e, f), some capsules fold (as visualized specifically in Fig. 4), which seems to disrupt their otherwise relatively ordered flow. This will be analyzed subsequently as a buckling mechanism, and the increased resistance this causes will be quantified as an effective viscosity. It can also be seen that the obvious cell-free layer in the smaller ξ_0 cases seems to disappear in this largest $\xi_0 = 3.0$ cases; this too is quantified in subsequent sections.

Fig. 3 Flow visualizations for $H_c = 0.25$, $W = 14r_0$ for $u^* = 0.2$ and $u^* = 1.0$ and $\xi_0 = 1.0, 1.7$ and 3.0 as labeled. For these visualizations $L = 30r_0$



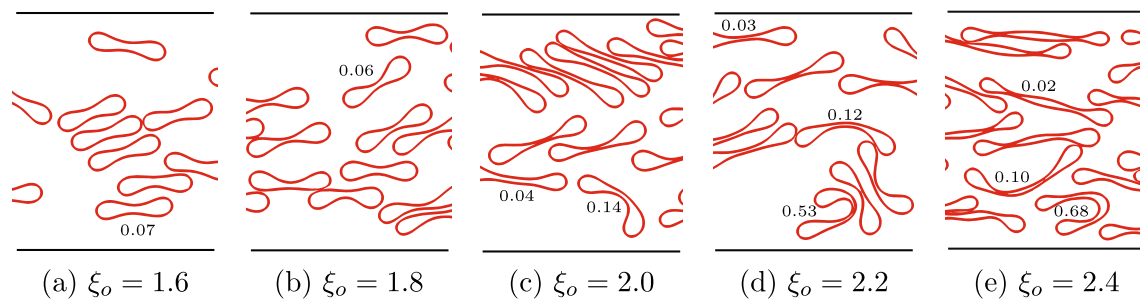


Fig. 4 Visualizations showing the onset of apparent buckling behavior for $H_c = 0.25$, $W = 14r_o$, $u^* = 1.0$ for ξ_o as labeled. The inset numbers indicate the buckling metric defined in “Buckling”

Macroscopic resistance: effective viscosity

The behavior of the capsules in flow for different ξ_o significantly alters the effective viscosity of the suspension,

$$\frac{\mu_{\text{eff}}}{\mu} = -\frac{W^2}{12\mu U} \left\langle \frac{dp}{dx} \right\rangle. \quad (12)$$

Reported values for μ_{eff} are time averages, which start after an apparently statistically stationary flow condition has been reached as quantified in Fig. 5. After an obvious transient, averaging is initiated once the instantaneous μ_{eff} varies by less than 2%. This condition is used for all cases reported.

We first consider $\xi_o = 1.6$, which best corresponds to healthy red blood cells and vary H_c and W , as in previous rheological studies of blood (Barbee and Cokelet

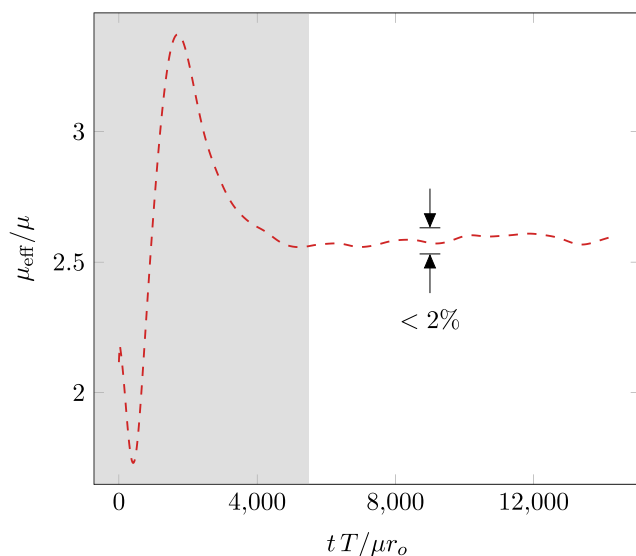
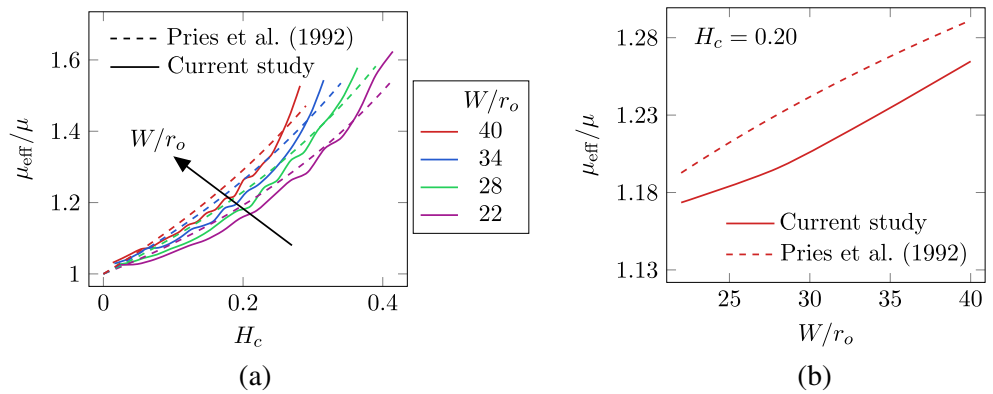


Fig. 5 Instantaneous μ_{eff} from Eq. 12 for $H_c = 0.25$, $W = 20r_o$ and $\xi_o = 2.4$. The nominally transient period is shaded, after which effective viscosity deviates by $< 2\%$

1971; Fahraeus and Lindqvist 1931). In Fig. 6a, effective viscosity is found to increase nonlinearly with H_c , in qualitative agreement with experimental results (Pries et al. 1992). Even a quantitative comparison with the corresponding empirical fits of Pries et al. (1992) is surprisingly good despite obvious approximations we make in applying the current configuration as a model for blood. In Fig. 6b, we see that the effective viscosity depends approximately linearly on channel width, which again agrees with experimental findings for blood, matching both the slope over the range of W considered and values are within 10%. It should be recognized in viewing these results that the present channels are several basic blood cell radii r_o across, and so we do not see the non-monotonic behavior that would be expected for vessels matching the capsule dimensions, though this too has been reproduced with similar capsule-scale simulations (Zhao et al. 2010).

Looking beyond this flow as a model of healthy blood, which might best correspond to $\xi_o = 1.6$, in Fig. 7, we see that there is significantly richer behavior when ξ_o is varied significantly. For all considered H_c , this nominal blood-like configuration $\xi_o \approx 1.6$ yields a local minimum μ_{eff} , with resistance increasing both toward smaller and larger ξ_o . The change is most pronounced for the largest $\xi_o \approx 3.0$ dog-bone geometries. In addition, capsules with $\xi_o \approx 1.6$ are also the least sensitive to changes of hematocrit: for $\xi_o = 1.6$, changing from $H_c = 0.05$ to 0.20 increases μ_{eff} by only a factor of 1.08, whereas it increases by a factor of 1.17 for $\xi_o = 1.0$ and by 1.73 for $\xi_o = 3.0$. We investigate the mechanisms underlying these observations in the remainder of the paper and start here by recalling that the visualizations in Fig. 3 suggest that the large ξ_o dog-bone shaped cells do not form any significant cell-free layer. It is well known that the presence of the cell-free layer decreases the effective viscosity of blood flow (Alonso et al. 1993; Alonso et al. 1995; Cokelet and Goldsmith 1991; Reinke et al. 1986; Reinke et al. 1987), which presents an obvious candidate mechanism for the seemingly rapid increase in μ_{eff} with ξ_o .

Fig. 6 Effective viscosity μ_{eff} from Eq. 12: **a** as a function of hematocrit for fixed channel width and **b** as a function of W for $H_c = 0.20$. Note that the dashed lines represent empirical fits of experimental data from Pries et al. (1992)



Capsule-free layer

We define the capsule-free layer thickness h to include 1 % of the collocation points representing the capsule membranes. All results are insensitive to this specific threshold; the boundary between the nominally capsule-free layer and the capsule-rich region is relatively sharp, and so changing this criterion to 15 % resulted in less than a 0.5 % change in h/W for typical cases. In Fig. 8, it is clear that $\xi_0 \approx 1.6$ discocyte geometries maximize the capsule-free layer thickness, which would indeed reduce μ_{eff} . We also see that faster flow (u^*) increases h for all cases with $\xi_0 \lesssim 2.0$, similar to experimental observations for red blood cells (Yamaguchi et al. 1992; Alonso et al. 1993; Alonso et al. 1995). For nearly circular capsules ($\xi_0 \lesssim 1.2$), h decreases modestly, consistent with experiments on hardened capsules and red blood cells (Simchon et al. 1987; Kozlovskaya et al. 2014). Most notable in Fig. 8, however, is that the sharp change to a much thinner layer for $\xi_0 \gtrsim 2.0$

suggests a fundamental change in the microstructural flow dynamics, which is investigated more thoroughly in the “Capsule orientation” section.

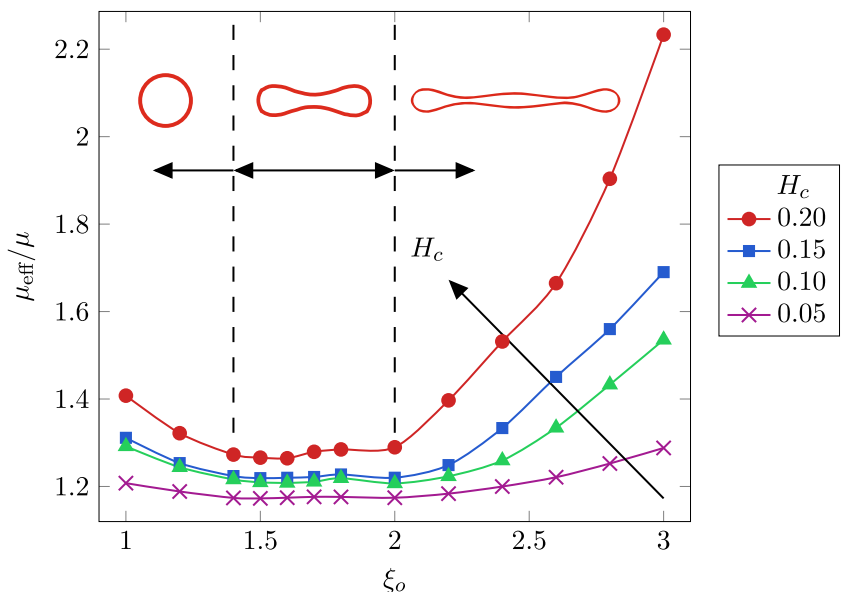
Capsule orientation

We begin our investigation of the capsule-scale flow structure by again considering the visualizations in Figs. 3 and 4, noting that the $\xi_0 \gtrsim 2.0$ capsules appear to have a tendency to fold, change orientation, and in certain cases apparently buckle. This seems to disrupt the relatively ordered arrangements of $\xi_0 \lesssim 2.0$ capsules, and corresponds with the apparent decrease of h . We start by considering the mean orientation angle and its variation in the different cases.

A nominal orientation is quantified based upon the orientation of a fitted ellipse determined by the eigensystem of

$$M_{ij} = \frac{1}{l} \int_l x'_i x'_j dS(\mathbf{x}), \tag{13}$$

Fig. 7 Effective viscosity for several different cases of H_c and ξ_0 , with $W/r_o = 20$ and $u^* = 1$



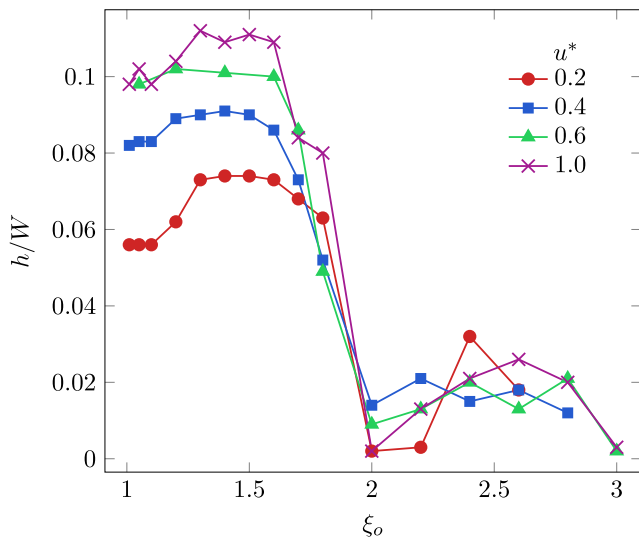


Fig. 8 Dependence of the capsule-free layer thickness on ξ_0 and capillary number u^* , shown for cases with $W/r_0 = 20$ and $H_c = 0.25$

where l is the capsule membrane length, and \mathbf{x}' is the surface position relative to the centroid: $\mathbf{x}' = \mathbf{x} - \mathbf{x}_c$. The eigenvalues $\lambda_{1,2}$ and corresponding eigenvectors $\mathbf{e}_{1,2}$ of M define a fitted ellipse,

$$\mathbf{x} = \sqrt{2\lambda_1}\mathbf{e}_1 \sin \psi + \sqrt{2\lambda_2}\mathbf{e}_2 \cos \psi, \tag{14}$$

where $\psi \in [0, 2\pi]$. The nominal orientation angle α is taken to be that between major axis of the ellipse and the normal to the channel wall (see Fig. 9).

The mean orientation $\langle \alpha \rangle$ changes significantly for different ξ_0 , as shown in Fig. 10. Nearly circular equilibrium geometries ($\xi_0 \approx 1.0$) on average orient with $\langle \alpha \rangle \approx 45^\circ$, corresponding to the visualization in Fig. 3. For $\xi_0 \approx 1.6$, corresponding to a discocyte type conformation, $\langle \alpha \rangle \approx 0$, which has been seen in experiments (McWhirter et al. 2009; Brust et al. 2014). However, the still more elongated dog-bone shapes deviate abruptly from this behavior, starting at $\xi_0 \approx 2.0$ and tend to orient themselves on average with $\langle \alpha \rangle \approx 15^\circ$. This sharp deviation is of similar character to both Figs. 7 and 8.

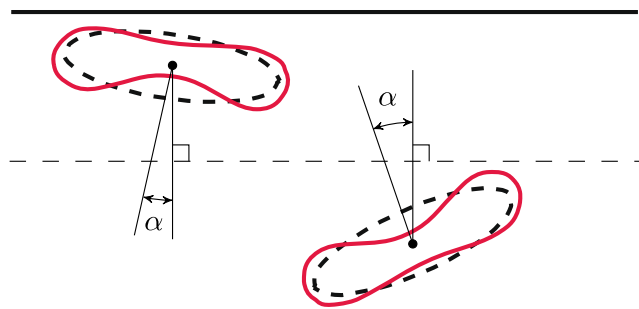


Fig. 9 Schematic of model capsules (solid) and their respective fitted ellipsoids (dashed)

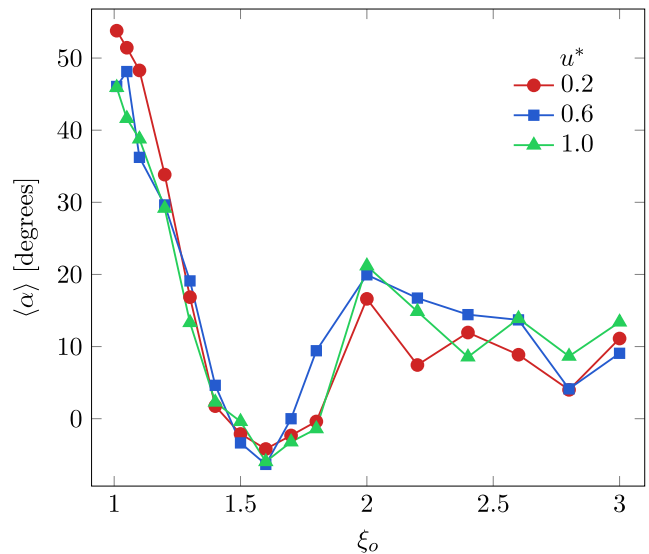


Fig. 10 Mean orientation angle for varied ξ_0 and flow strengths u^* . $H_c = 0.25$ and $W/r_0 = 20$ for all cases

The visualizations in Fig. 3 also suggest that the orientations also become more varied for $\xi_0 \gtrsim 2.0$ as the capsules fold and appear to tumble, which we quantify with the orientation variance

$$\sigma_\alpha = \left\langle \alpha_i - \langle \alpha \rangle \right\rangle^{1/2}. \tag{15}$$

Anticipating that σ_α depends on an apparent buckling-like mechanism discussed in “Buckling”, which in turn is

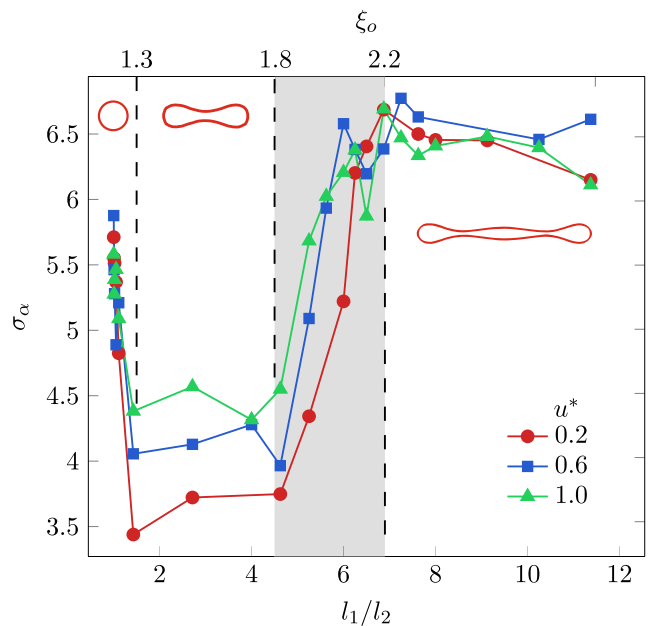
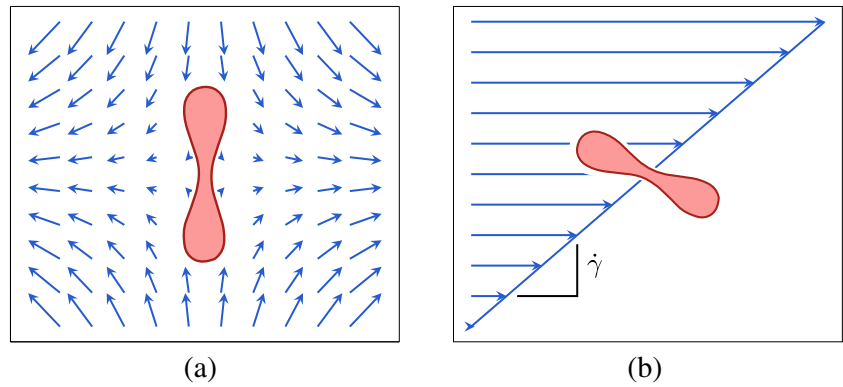


Fig. 11 Variance of orientation angle σ_α as a function of configuration aspect ratio and capillary number for $W/r_0 = 20$ and $H_c = 0.25$. The vertical dashed lines represent approximate geometry and behavioral regimes as indicated

Fig. 12 Auxiliary flow configurations: (a) capsules in a Taylor–Green stagnation point flow and (b) homogeneous shear



expected to be sensitive to the aspect ratio (slimness ratio) of the capsules, we plot the orientation variance against the aspect ratio of the rest configurations of the capsules: l_1/l_2 . This is shown in Fig. 11, and it is clear that there is a significant and sudden increase in orientation angle variance in the range $4.5 \lesssim l_1/l_2 \lesssim 6.5$, which corresponds to $1.8 \lesssim \xi_0 \lesssim 2.2$. There is also an increase in σ_α for small ξ_0 , which have $l_1/l_2 \approx 1$, but this is less consequential because l_1 and l_2 are nearly the same for small ξ_0 , and presumably due to the fact that relatively minor perturbations can change the nominal orientation of an ellipse fitted to a nearly round capsule.

Buckling

To explore the apparent buckling of the capsules in channel flow, we consider it in two more idealized flow configurations. The first is a Taylor–Green flow (Fig. 12a), with velocity components

$$U_x = A \sin\left(\frac{2\pi}{L}x\right) \cos\left(\frac{2\pi}{L}y\right), \tag{16}$$

$$U_y = -A \cos\left(\frac{2\pi}{L}x\right) \sin\left(\frac{2\pi}{L}y\right), \tag{17}$$

where A is the flow strength and $L = 80r_0$ is the periodic length of the square domain; it was confirmed that results were independent of this computational domain within $\pm 40r_0$. A single capsule is placed vertically at the stagnation, such that it will be compressed by the flow as shown in Fig. 12a. A small perturbation is applied to the shape of the membrane just before the flow is imposed with

$$x_{\text{pert}} = x + \varepsilon \sin^{10}\left(\frac{y\pi}{l_1}\right), \tag{18}$$

where $\varepsilon = 0.01r_0$ and as before l_1 is the longest at-rest membrane dimension. In this flow, the magnitude of the relevant velocity scale is given by the velocity difference across the capsule. The second flow is the homogeneous shear shown in Fig. 12b, which was imposed in the usual way (Zhou and Pozrikidis 1995; Metsi 2000). The relevant

velocity scale is again given by the velocity drop across the capsule; in the case of homogeneous shear, this is $U_{\text{shear}} = \dot{\gamma}\ell$ where $\dot{\gamma}$ is the shear rate and ℓ is the vertical distance across the capsule. The capsule is initialized in its equilibrium shape and positioned at 25° from the horizontal (as shown in Fig. 9), though we verify that our results produce a consistent onset of buckling for deviations of $\pm 15^\circ$ of this initial angle.

The visualizations of Figs. 3 and 4 show several examples of nominally buckled capsules. This is quantified based upon the principal axes of the fitted ellipses: $\lambda \equiv \lambda_1/\lambda_2$, where λ_r is the equilibrium value for a particular ξ_0 . A buckled capsule will transition from elongated ($\lambda \approx \lambda_r$) to larger λ , up to $\lambda \lesssim 1$. Some example λ values for different shapes are included in the visualizations of Fig. 4).

We see in Fig. 13 that an example $\lambda(t)$ history for a $\xi_0 = 2.6$ capsule has four large spikes, each reaching near $\lambda = 1$, indicating four buckling events. This behavior is typical of

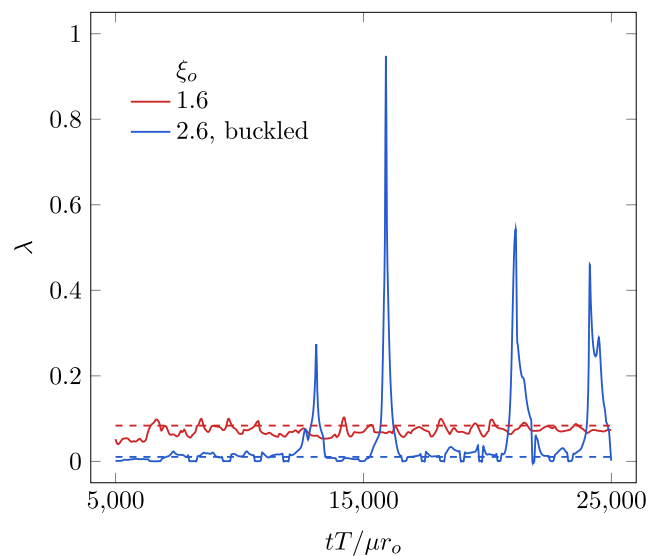
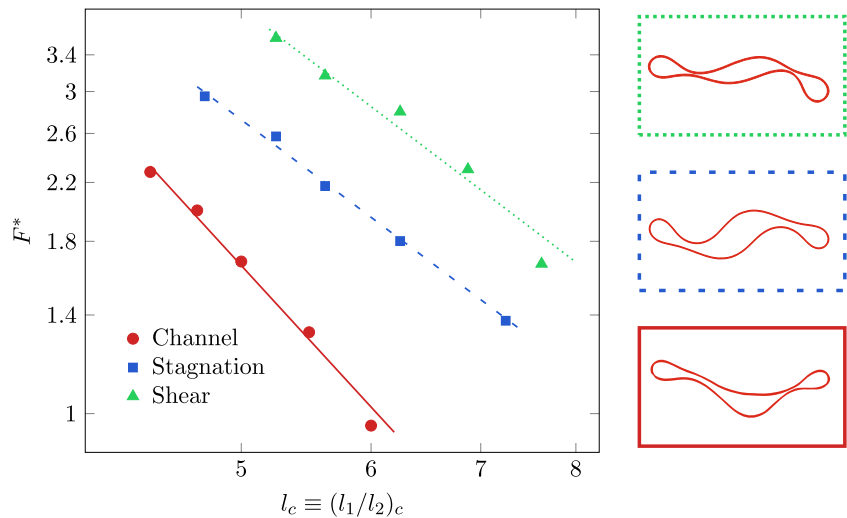


Fig. 13 Buckling parameter $\lambda \equiv \lambda_1/\lambda_2$ from Eq. 14 for representative biconcave $\xi_0 = 1.6$ capsule and a dog-bone shaped $\xi = 2.6$ capsule. Dashed lines show the equilibrium $\lambda = \lambda_r$ condition. In both cases, $H_c = 0.25$, $u^* = 1.0$ and $W = 20r_0$

Fig. 14 Scaling of critical buckling aspect ratio due to forcing F^* due to the fluid. Visualizations show buckling examples from the different flow fields for $\xi_0 = 2.8$, $u^* = 1$. The channel has $W/r_0 = 20$ and $H_c = 0.25$. The straight lines are power-law fits $F^* \sim l_c^{-b}$ with $b = 2.65$ for the channel, 1.82 for the stagnation flow, and 1.82 for the homogeneous shear



these capsules. During the course of the simulations nearly all dog-bone geometry capsules are observed to buckle at least once, and typically about 20 % of them are buckled at any given time. A corresponding biconcave $\xi_0 = 1.6$ case also shown in Fig. 13 has a nearly constant λ for its entire history. To provide a specific metric, we take $\lambda \geq 5\lambda_r$ to be buckled.

To compare the different configurations, we defined a non-dimensional critical force, $F^* \equiv F/\mu U l_0$ where U is the relevant velocity scale as described previously. For Euler buckling, this should scale as $F^* \approx 1/l_c^2$, though there is no expectation that the present capsules should exactly follow this criterion developed for solid long, slender objects. Indeed, one might anticipate that the model capsules would be better described as approximately axially loaded shells, which have a power-law buckling threshold l_c^{-b} with $1 < b < 2$ (Lancaster et al. 2000; Bushnell 1981). In Fig. 14, for the stagnation point flow, we find $F^* \sim l_c^{-1.82}$ and for the shear flow $F^* \sim l_c^{-1.84}$. The channel flow shows more ready buckling, with $l_c^{-2.65}$, possibly due to the finite-amplitude disturbances arising from capsule-capsule and capsule-wall interactions. Studies of red blood cells show in-plane reversible buckling of healthy cells does occur in an optical trap (Ghosh et al. 2006).

Influence of buckled capsules and their kinematics

Buckling behavior also corresponds to a fundamental change in other kinematic behavior of the capsules. Figure 15a and b contrast the $y-t$ trajectories of five arbitrarily selected capsules for $\xi_0 = 2.6$ and $\xi_0 = 1.6$ cases. It is clear that the $\xi_0 = 2.6$ capsules undergo much more lateral migration than the $\xi_0 = 1.6$ capsules. The buckled capsules appear to roll in the flow, which is confirmed by plotting their orientation angle history $\alpha(t)$, as computed in the “Capsule orientation” section, in Fig. 15c, d. In Fig. 15c, a

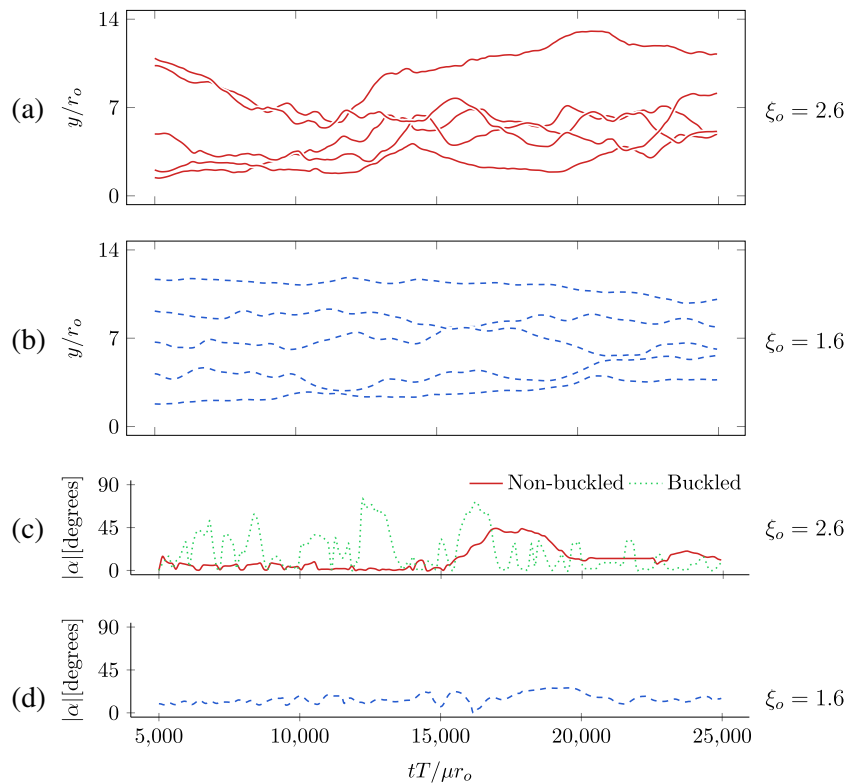
$\xi_0 = 2.6$ capsule that repeatedly buckles (based on $\lambda > 5\lambda_r$) continually changes angle relative to one that does not. These sudden changes of orientation seem to cause disruptions in the flow, which have consequences of increased interactions with nearby capsules, apparent reduction of capsule-free layer thickness, and an increase of effective viscosity. For the corresponding non-buckling $\xi_0 = 1.6$ case, the capsule angles are typically much less varied (Fig. 15d).

We statistically analyze the overall behavior associated with the specific examples of Fig. 15 by computing the average transverse velocity of the capsules, \dot{y} . This provides a measure for the lateral migration of different capsule geometries. We also quantify the mean absolute transverse distance traveled,

$$\Delta_y = \frac{1}{N} \sum_{i=1}^N \max_{j,k} |y_i(t_j) - y_i(t_k)|, \tag{19}$$

as another measure of this. It should be noted that Δ_y , as defined, is dependent upon the time over which (19) is calculated; here, a capsule advected at speed U would have traveled a streamwise distance of $18L/r_0$. In Fig. 16 there is an apparent jump to large Δ_y and $\langle \dot{y} \rangle$ for $\xi_0 \gtrsim 2.0$, which agrees with a similar distinct behavior shown in Fig. 15 and particularly Fig. 11, which shows the rapid increase in capsule-angle variance for $\xi_0 \approx 1.9$. This seems to be an evident change in mechanism where the behavior of $\langle \dot{y} \rangle$ and Δ_y scale approximately logarithmically for circular and biconcave geometries, but are constant for elongated capsules ($\xi_0 \gtrsim 2.0$). For the cases simulated in Fig. 15, it is found that capsules that buckle during the course of the simulation experience approximately 1.4 times more vertical migration as an average non-buckling capsule (see Fig. 15), which then have a proportionally larger hydrodynamic influence on other capsules in the flow.

Fig. 15 Transverse position for five representative biconcave and dog-bone capsules with $H_c = 0.25$, $W/r_o = 14$ and $u^* = 1.0$. The orientation history of a buckled (c, *dotted*) versus non-buckled dog-bone capsule (c, *solid*) are shown as defined (see text), as well as the orientation of a biconcave capsule (d)



Hydrodynamic interactions

The kinematic observations of the previous subsection suggest that large ξ_o capsules buckle more readily, leading to a rolling motion and greater transverse transport. Though the interaction dynamics are intricate, we can quantify some of their basic characteristics through multipole moments

of the capsules hydrodynamic influence (Pozrikidis 1992; Guazzelli and Morris 2012). These are defined by expanding the Stokeslet S_{ij} in Eq. 8 about the capsule centroid $\mathbf{x}' = 0$,

$$S_{ij}(\mathbf{x} - \mathbf{x}') = S_{ij}(\mathbf{x}) - x'_k \frac{\partial S_{ij}}{\partial x_k}(\mathbf{x}) + \dots, \tag{20}$$

where \mathbf{x} is a point far from the capsule such that $|\mathbf{x}| \gg |\mathbf{x}'|$. When substituted into the boundary integral equation (7), this reduces to

$$u_i(\mathbf{x}) - U_i(\mathbf{x}) = -\frac{F_j}{8\pi\mu} S_{ij}(\mathbf{x}) + \frac{Q_{jk}}{8\pi\mu} \frac{\partial S_{ij}}{\partial x_k}(\mathbf{x}) + \dots, \tag{21}$$

where F_j is the hydrodynamic drag force and Q_{jk} is the first moment of the traction about the capsule membranes Ω ,

$$Q_{jk} = \int_{\Omega} (\sigma_{jl} n_l) x'_k ds. \tag{22}$$

Splitting Q_{jk} into its symmetric and skew-symmetric parts,

$$Q_{jk} = G_{jk} + R_{jk}, \tag{23}$$

yields the symmetric stresslet G_{jk} and skew-symmetric rotlet R_{jk} , which is associated with the hydrodynamic torque. These provide a means of estimating to leading order the contribution of stress and rotation to the hydrodynamic influence of each capsule.

In Fig. 17, we plot the matrix norms $\|\mathbf{G}\| = \sqrt{G_{ij}G_{ji}}$ and $\|\mathbf{R}\| = \sqrt{R_{ij}R_{ji}}$ for increasing ξ_o . The leading-order stresslet contribution has a minimum for nearly circular

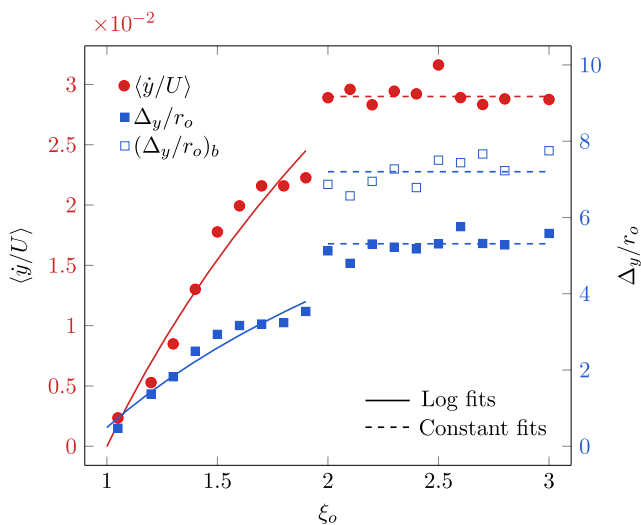


Fig. 16 The average transverse velocity of the capsules (\dot{y}/U) and transverse displacement Δ_y/r_o from Eq. 19. We also show Δ_y for exclusively capsules that have buckled at least once during the course of the simulation, $(\Delta_y/r_o)_b$

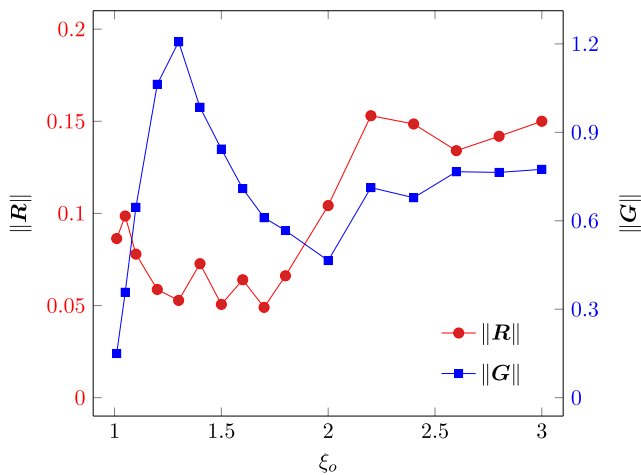


Fig. 17 Stresslet G_{ij} and rotlet R_{ij} strengths for different ξ_0 for $H_c = 0.20$, $u^* = 1$ and $W = 20r_0$

capsules $\xi_0 \approx 1.0$, as expected because they are compact and seemingly interact with the flow the least (see Fig. 16), and more interestingly a local minimum at $\xi_0 \approx 2.0$. At this point, it seems that potential tank-treading motions are balanced by the tumbling behavior of elongated capsules. Hydrodynamic interactions are then minimized for very nearly circular geometries, and locally small for biconcave $1.5 \lesssim \xi_0 \lesssim 2.0$ configurations. This seems to have the implication that capsules with $1.2 \lesssim \xi_0 \lesssim 1.5$ have decreasing resistance to traveling through narrow confines. In contrast, R_{ij} becomes relatively stronger only for $\xi_0 \gtrsim 2.0$ due to the elongated capsule membrane and corresponds to the onset of buckling and increasing effective viscosity.

Conclusions

The role of capsule reduced area was studied in regard to the dynamics of capsule suspensions flowing in narrow confines. A two-dimensional model system was studied, so no quantitative one-to-one correspondence is expected with actual three-dimensional capsules systems. However, its success at reproducing important known phenomena suggests that it can be informative for realistic configurations, including blood flow.

The principal observation was a sudden change in the suspension behavior for capsules with membranes with equilibrium lengths about twice that of the minimum ($\xi_0 \approx 2.0$). This was manifested in the overall rheology as quantified by a significant jump of the effective viscosity of the suspension. Corresponding changes observed at the capsule scale for $\xi_0 \gtrsim 2.0$ were a significantly diminished cell-free-layer thickness, significant variation in the capsule orientation, increased lateral transport, and increased leading-order rotlet contribution to the multipole expansion.

These observations corresponded to the onset of a buckling behavior, which were shown to scale with capsule aspect ratio consistent with expectations for shell membranes.

Acknowledgments This work was supported in part by the National Science Foundation under Grant No. CBET 13-36972.

References

- Alonso C, Pries AR, Gaehtgens P (1993) Time-dependent rheological behavior of blood at low shear in narrow vertical tubes. *Am J Physiol Heart Circ Physiol* 265:553–561
- Alonso C, Pries AR, Kiesslich O, Lerche D, Gaehtgens P (1995) Transient rheological behavior of blood in low-shear tube flow: velocity profile and effective viscosity. *Am J Physiol Heart Circ Physiol* 268:25–32
- Anderson R, Cassell M, Mullinax GL, Chaplin Jr. H (1963) Effect of normal cells on viscosity of sickle-cell blood. *Arch Intern Med* 111:286–294
- Barbee JH, Cokelet GR (1971) Prediction of blood flow in tubes with diameters as small as 29 μ . *Microvasc Res* 3:17–21
- Bishop JJ, Popel AS, Intaglietta M, Johnson PC (2001) Rheological effects of red blood cell aggregation in the venous network: a review of recent studies. *Biorheology* 38:263–274
- Brezavsek AH, Rauzi M, Leptin M, Zihlerl P (2012) A model of epithelial invagination driven by collective mechanics of identical cells. *Biophysics* 103:1069–1077
- Bronzino JD (2000) The biomedical engineering handbook. IEEE Press/CRC Press, Boca Raton
- Brust M, Aouane O, Thiébaud M, Flormann D, Verdier C, Kaestner L, Laschke MW, Selmi H, Benyoussef A, Podgorski T, Coupié G, Misbah C, Wagner C (2014) The plasma protein fibrinogen stabilizes clusters of red blood cells in microcapillary flows. *Sci Rep*:4
- Bugliarello G, Sevilla J (1970) Velocity distribution and other characteristics of steady and pulsatile blood flow in fine glass. *Biorheology* 7(2):85–107
- Bushnell D (1981) Buckling of shells—pitfall for designers. *AIAA J.* 19(9):1183–1226
- Calle LM, Li WN, Buhrow JW, Perusich SA, Jolley ST, Gibson TL, Williams MK (2012) Elongated microcapsules and their formation. *US Patent App.* 13/354,576
- Canham PB (1970) The minimum energy of bending as a possible explanation of the biconcave shape of the human red blood cell. *J Theoret Biol* 26:61–81
- Cantat I, Misbah C (1999) Lift force and dynamical unbinding of adhering vesicles under shear flow. *Phys Rev Lett* 83(4):880–883
- Chabanel A, Reinhart W, Chien S (1987) Increased resistance to membrane deformation of shape-transformed human red blood cells. *Blood* 69:739–743
- Chang TM (2010) Blood replacement with nanobiotechnologically engineered hemoglobin and hemoglobin nanocapsules. *Wiley InterSci Rev Nanomed Nanobiotechnol* 2:418–430
- Clausen JR, Reasor Jr. DA, Aidun CK (2011) The rheology and microstructure of concentrated non-colloidal suspensions of deformable capsules. *J Fluid Mech* 685:202–234
- Cokelet GR (1972) The rheology of human blood. Prentice-Hall
- Cokelet GR, Goldsmith HL (1991) Decreased hydrodynamic resistance in the two-phase flow of blood through small vertical tubes at low flow rates. *Circ Res* 68:1–17
- Da Costa L, Galimand J, FenetEAU O, Mohandas N (2013) Hereditary spherocytosis, elliptocytosis, and other red cell membrane disorders. *Blood Rev* 27(4):167–178

- Dey NS, Majumdar S, Rao MEB (2008) Multiparticulate drug delivery systems for controlled release. *Trop J Pharm Res* 7(3):1067–1075
- Distenfass L (1968) Internal viscosity of the red cell and a blood viscosity equation. *Nature* 219:956–958
- Donbrow M (1991) Microcapsules and nanoparticles in medicine and pharmacy. CRC Press
- d’Onofrio G, Zini G (2014) Morphology of blood disorders. Wiley
- Emmel VE (1917) A study of the erythrocytes in a case of severe anemia with elongated and sickle-shaped red blood corpuscles. *Archives of Internal Medicine, University of Illinois College of Medicine* 20:586–598
- Fahraeus R, Lindqvist T (1931) The viscosity of the blood in narrow capillary tubes. *Am J Physiol* 96:562–568
- Fedosov DA, Dao M, Karniadakis GE, Suresh S (2014) Computational biorheology of human blood flow in health and disease. *Ann Biomed Eng* 42(2):368–387
- Firrell JC, Lipowsky HH (1989) Leukocyte margination and deformation in mesenteric venules of ram. *Am J Physiol Heart Circ Physiol* 225(6):1667–1674
- Freund JB (2007) Leukocyte margination in a model microvessel. *Phys Fluids* 19(023301)
- Freund JB (2014) Numerical simulations of flowing blood cells. *Annu Rev Fluid Mech* 46:67–95
- Freund JB, Orescanin MM (2011) Cellular flow in a small blood vessel. *J Fluid Mech* 671:466–490
- Freund JB, Zhao H (2010) Hydrodynamics of Capsules and Biological Cells, chapter A fast high-resolution boundary integral method for multiple interacting blood cells. Chapman and Hall/CRC, Boca Raton, pp 71–111
- Ghigliotti G, Biben T, Misbah C (2010) Rheology of a dilute two-dimensional suspension of vesicles. *J Fluid Mech* 653:489–518
- Ghosh A, Sinha S, Dharmadhikari JA, Roy S, Dharmadhikari AK, Samuel J, Sharma S, Mathur D (2006) Euler buckling-induced folding and rotation of red blood cells in an optical trap. *Phys Biol* 3:67–73
- Gibbs BF, Kermasha S, Alli I, Mulligan CN (1999) Encapsulation in the food industry: a review. *Int J Food Sci Neut* 50:213–224
- Guazzelli E, Morris JF (2012) A physical introduction to suspension dynamics. Cambridge Texts in Applied Mathematics. Cambridge University Press
- Hasimoto H (1959) On the periodic fundamental solutions of the Stokes equations and their application to viscous flow past a cubic array of spheres. *J Fluid Mech* 5(2):317–328
- Isfahani AHG (2008) A 2d stokes suspension solver with application to red blood cell phenomenology. Master’s thesis, University of Illinois at Urbana-Champaign
- Jan KM, Chien S (1973) Role of surface electric charge in red blood cell interactions. *J Gen Physiol* 61(638)
- Jenkins JT (1977) Static equilibrium configurations of a model red blood cell. *J Math Biol* 4:149–169
- Kim S, Karrila SJ (1991) Microhydrodynamics: principles and selected applications. Butterworth-Heinemann, Boston
- Knoche S, Kierfeld J (2011) Buckling of spherical capsules. *Phys Rev E* 84(046608)
- Kozlovskaya V, Alexander JF, Wang Y, Kunczewicz T, Liu X, Godin B, Kharlampieva E (2014) Internalization of red blood cell-mimicking hydrogel capsules with pH-triggered shape responses. *ACS Nano* 8(6):5725–5737
- Kumar A, Henriquez Rivera RG, Graham MD (2014) Flow-induced segregation in confined multicomponent suspensions: effects of particle size and rigidity. *J Fluid Mech* 738:423–462
- Lancaster ER, Calladine CR, Palmer SC (2000) Paradoxical buckling behavior of a thin cylindrical shell under axial compression. *Int J Mech Sci* 42:843–865
- Lei H, Fedosov DA, Caswell B, Karniadakis GE (2013) Blood flow in small tubes: quantifying the transition to the non-continuum regime. *J Fluid Mech* 722:214–239
- Li X, Vlahovska PM, Karniadakis GE (2013) Continuum- and particle-based modeling of shapes and dynamics of red blood cells in health and disease. *Soft Matter* 9:28–37
- Majeti NV, Kumar R (2000) Nano and microparticles as controlled delivery devices. *J Pharm Sci* 3(2):234–258
- Martini P, Pierach A, Schreyer E (1930) Die stromung des blutes in engen gefassen. eine abweichung vom poiseuille’schen gesetz. *Dtsch Arch KZin Med* 169:212–222
- McWhirter JL, Noguchi H, Gompper G (2009) Flow-induced clustering and alignment of vesicles and red blood cells in microcapillaries. *Proc Natl Acad Sci* 106(15):6039–6043
- Metsi E (2000) Large scale simulations of bidisperse emulsions and foams. PhD thesis, University of Illinois at Urbana-Champaign
- Paret N, Trachsel A, Berthier DL, Herrmann A (2015) Controlled release of encapsulated bioactive volatiles by rupture of the capsule wall through the light-induced generation of a gas. *Chem Int Ed* 54(7):2275–2279
- Peyratout CS, Dahne L (2004) Taylor-made polyelectrolyte microcapsules: from multilayers to smart containers. *Angew Chem Int Ed* 43:3762–3783
- Pop F (2011) Chemical stabilization of oils rich in long-chain polyunsaturated fatty acids during storage. *Food Sci Technol Int* 17(2):111–117
- Pozrikidis C (1992) Boundary integral and singularity methods for linearized viscous flow. Cambridge University Press
- Pozrikidis C (2001) Effect of membrane bending stiffness on the deformation of capsules in simple shear flow. *J Fluid Mech* 440:269–291
- Pries AR, Neuhaus D, Gaetgens P (1992) Blood viscosity in tube flow: dependence on diameter and hematocrit. *Am J Physiol*:263
- Raghunathan Y, Amsel L, Hinsvark O, Bryant W (1981) Sustained-release drug delivery system I: coated ion-exchange resin system for phenylpropanolamine and other drugs. *J Pharm Sci* 70:379–384
- Rahimian A, Veerapaneni SK, Biros G (2010) Dynamic simulation of locally inextensible vesicles suspended in an arbitrary two-dimensional domain, a boundary integral method. *J Comp Phys* 229:6466–6484
- Reinke W, Gaetgens P, Johnson PC (1987) Blood viscosity in small tubes: effect of shear rate, aggregation, and sedimentation. *Am J Physiol Heart Circ Physiol* 253:540–547
- Reinke W, Johnson PC, Gaetgens P (1986) Effect of shear rate variation on apparent viscosity of human blood in tubes of 29–94 μm . *Circ Res* 59:124–132
- Henriquez Rivera RG, Sinha K, Graham MD (2015) Margination regimes and drainage transition in confined multicomponent suspensions. *Phys Rev Lett*:114
- Sankar DS, Lee U (2008) Two-fluid Herchel-Bilkey model for blood flow in catheterized arteries. *J Mech Sci Tech* 22(5):1008–1018
- Sharan M, Popel AS (2001) A two-phase model for flow of blood in narrow tubes with increased effective viscosity near the wall. *Biorheology* 38(5-6):415–428
- Shiga T, Maeda N, Kon K (1990) Erythrocyte rheology. *Oncology/Hematology* 10:9–48
- Simchon S, Jan K, Chien S (1987) Influence of reduced red cell deformability on regional blood flow. *Am J Physiol Heart Circ Physiol* 253(22):898–902
- Skalak R, Ozkaya N, Skalak TC (1989) Biofluid mechanics. *Annu Rev Fluid Mech* 21:167–204
- Smith JE, Mohandas N, Clark MR, Greenquist AC, Shohet SB (1980) Deformability and spectrin properties in three types of elongated red cells. *Am J Hematol* 8:1–13

- Srivastava VP (2007) A theoretical model for blood flow in small vessels. *Int J App App Math* 2(1):51–65
- Staben ME, Zinchenko AZ, Davis RH (2003) Motion of a particle between two parallel plane walls in low-Reynolds-number Poiseuille flow. *Phys Fluids* 15:1711
- Ulbricht M (2006) Advanced functional polymer membranes. *Polymer* 47(2):2217–2262
- Wang Y, Bansal V, Zelikin AN, Caruso F (2008) Templated synthesis of single-component polymer capsules and their application in drug delivery. *Nano Lett* 8(6):1741–1745
- Weinbaum S, Ganatos P (1990) Numerical multipole and boundary integral equation techniques in Stokes flow. *Annu Rev Fluid Mech* 22:275–316
- Whitmore RL (1968) *Rheology of the circulation*. Pergamon, Oxford
- Yamaguchi S, Yamakawa T, Niimi H (1992) Cell-free plasma layer in cerebral microvessels. *Biorheology* 29:251–260
- Zhao H, Isfahani AHG, Olson L, Freund JB (2010) A spectral boundary integral method for micro-circulatory cellular flows. *J Comp Phys* 229:3726–3744
- Zhao H, Shaqfeh ESG (2011) Shear-induced platelet margination in a microchannel. *Phys Rev E* 83(6)
- Zhou H, Pozrikidis C (1995) Deformation of liquid capsules with incompressible deformation of liquid capsules with incompressible interfaces in simple shear flow. *J Fluid Mech* 283:175–200